Fabrication and characterization of uranium–thorium–zirconium hydrides

Kurt A. Terrani [a,*], G.W. Chinthaka Silva [b], Charles B. Yeamans [a], Mehdi Balooch [a], Donald R. Olander [a]

[a] Department of Nuclear Engineering, University of California, 4155 Etcheverry Hall, M.C. 1730, Berkeley, CA 94720-1730, USA
[b] Harry Reid Center for Environmental Studies, University of Nevada Las Vegas, Box 454009, Las Vegas, NV 89154, USA

ABSTRACT

Two uranium–thorium–zirconium hydrides, $(UTh_4Zr_{10})H_{1.9}$ and $(U_4Th_2Zr_9)H_{1.5}$, have been fabricated and characterized. Fabrication involved arc melting of the constituent pure metals to form homogenous alloys, followed by hydriding at elevated temperatures in a hydrogen gas environment. The compounds were characterized by X-ray powder diffractometry as well as scanning and transmission electron microscopy. These methods revealed a multi-phase mixture of δ-zirconium hydride ($ZrH_{1.6+x}$), thorium–zirconium hydride ($ThZr_2H_{7-x}$), and uranium metal. The elastic modulus was mapped across the microstructure using nanoscale dynamic stiffness mapping. The elastic modulus of $ThZr_2H_{7-x}$ phase is found to be 172 GPa.

Published by Elsevier B.V.

1. Introduction

Hydride nuclear fuels consist of metallic uranium particles dispersed in a hydride matrix. In the case of TRIGA fuel, the matrix consists solely of the δ-zirconium hydride ($ZrH_{1.6}$) phase. Hydride matrices have higher hydrogen atomic densities compared to PWR or BWR coolants, and act as effective moderators to enhance the thermalization of neutrons in fission reactors. This allows more compact core designs with higher power density, since a considerable fraction of the water moderator can be replaced with hydrogen within the fuel. In addition to higher thermal conductivity compared to the oxide fuels, hydride fuels also exhibit thermally-induced hydrogen up-scattering that accompanies Doppler feedback, which in turn provides a negative prompt temperature coefficient of reactivity [1].

Uranium–thorium–zirconium hydride fuel has been proposed as an optimized matrix for the deep burn of plutonium and minor actinides [2–5]. The proposed fuel could achieve TRU (transuranic elements) destruction fractions as high as twice those realized with MOX (mixed oxide) fuel. Unlike MOX fuel, it is also possible to realize infinite cycles of partitioning and transmutation with the hydride fuel without the risk of large positive reactivity coefficients as the cycles progress [6].

Two uranium–thorium–zirconium hydride fuels of the overall chemical formulae $(UTh_4Zr_{10})H_{1.9}$ and $(U_4Th_2Zr_9)H_{1.5}$ have been fabricated in order to investigate and characterize the microstructure and the corresponding phases forming the material. $(UTh_4Zr_{10})H_{1.9}$ fuel is chosen as a benchmark based on previous work performed by Yamamoto et al. [7]. The $(U_4Th_2Zr_9)H_{1.5}$ fuel

is on the other hand selected based on the studies carried out by Ganda and Greenspan [1,5] where the fuel composition is optimized to achieve the longest possible fuel cycle while maintaining negative reactivity coefficients.

2. Fuel fabrication

Fuel fabrication was performed in Idaho National Laboratory's Materials and Fuels Complex. All the fabrication activities were performed either inside fume hoods with continuous air monitoring or in negative-pressure gloveboxes.

Two alloys of uranium–thorium–zirconium were prepared by arc melting of high-purity metal feedstock (>99%) in an argon glovebox with less than 4 ppm oxygen. The alloys were subsequently cast in the shape of pins each weighing roughly 30 g. The metals were initially acid treated so that any impurities and scales on the surface were removed. Arc melting was done through the arc-lift process where the solidified buttons were turned five times and re-melted to achieve good homogeneity. Between each melting step, the surface of the button was abraded to remove impurities agglomerated at the surface. Arc melting resulted in melt temperatures in excess of 4000 °C. The melt (single phase liquid) was then quickly solidified on a copper hearth, resulting in a quenched microstructure with dendrite formation. According to the ternary phase diagram of the uranium–thorium–zirconium system [8], both of the alloys at equilibrium are in the $\gamma(U + Zr) + \alpha$-Th two phase region. The γ phase is a solid solution of uranium and zirconium with a body-centered cubic unit cell, whereas the α-thorium phase has a face-centered cubic unit cell.

The arc-melted alloys were cut into disks of 2 mm thickness prior to hydriding in order to reduce the diffusion path length of hydrogen (diffusion-limited hydriding kinetics are assumed). The

* Corresponding author. Tel.: +1 510 642 4077; fax: +1 510 643 9685.
  E-mail address: terrani@berkeley.edu (K.A. Terrani).
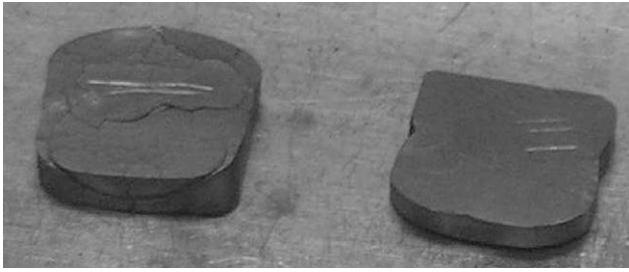
Fig. 1. $(UTh_4Zr_{10})H_{1.9}$ fuel disks. The disk to the left has experienced cracking due to severe volume expansion.

Table 1
Detailed composition and calculated densities for $(UTh_4Zr_{10})H_{1.9}$ and $(U_4Th_2Zr_9)H_{1.5}$ fuels.

	$(UTh_4Zr_{10})H_{1.9}$	$(U_4Th_2Zr_9)H_{1.5}$
Theoretical H/M[a] ratio	2.08	1.47
Theoretical H/(Zr + Th) ratio	2.23	2.00
Actual H/M ratio	1.93	1.55
Actual H/(Zr + Th) ratio	2.07	2.11
Vol.% α-U	4.49	20.14
Vol.% δ-ZrH$_{1.6}$	11.75	32.92
Vol.% ThZr$_2$H$_{7-x}$	83.76	46.93
Fuel density (g/cm^3)	7.57	9.10

^{a} M = U + Th + Zr.

metal disks underwent hydriding in a conventional tube furnace under 1 atm of hydrogen gas for 4 h. Furnace temperature was initially set at 900 °C and was gradually reduced to 500 °C over the hydriding period. Since the hydriding process is diffusion-limited, high temperatures were advantageous. Also, the material was able to better withstand the increase in volume at higher temperatures while maintaining its physical integrity. On the other hand, the furnace temperature had to be reduced eventually in order to increase the activity of hydrogen in the solid phase, and thus achieve higher hydrogen-to-metal (H/M) ratios. Typical disks after hydriding are shown in Fig. 1.

The detailed composition of the fuels is presented in Table 1. Actual H/M ratios were determined by weighing the samples prior to and after the hydriding process. The theoretical H/M ratios are calculated based on the assumption that the two hydride phases forming the fuels are δ-ZrH$_{1.6+x}$ and ThZr$_2$H$_{7-x}$ while the uranium remains metallic (α-U). Volume fractions of each phase and the fuel density are all calculated based on the crystal structure of the aforementioned three different phases in the fuel. The theoretical density of the $(UTh_4Zr_{10})H_{1.9}$ is in good agreement with the experimental value of 7.55 g/cm^3 determined by Tsuchiya et al. [9].

3. Characterization

3.1. X-ray diffractometry (XRD)

XRD samples were prepared by depositing fuel powder on a low background silicon single-crystal sample holder using a slurry of

powder and ethanol. Samples were also mixed with lanthanum hexaboride (LaB$_6$ SRM 660a) powder to be used as an internal standard during pattern refinement. High-resolution diffraction patterns were obtained using a Phillips PANalytical X'Pert Pro instrument with a Cu Kα source.

Rietveld refinement was performed on the experimental patterns for the two fuels. Formation of ThZr$_2$H$_{7-x}$, δ-ZrH$_{1.6+x}$, α-U, and minute amounts of ε-UH$_3$ was confirmed. Detailed results are presented in Table 2. The lattice parameter of α-U and ε-UH$_3$ phases could not be accurately determined for the $(UTh_4Zr_{10})H_{1.9}$ fuel due to the small volume fraction of these phases in this fuel. None of the following phases (accompanied by the corresponding space group) were detected in either of the fuels: ε-ZrH$_{1.8-x}$ (I4/mmm); δ-UH$_3$ (Pm-3n); δ-UZr$_2$ (P6/mmm); ZrH (P42/n); ThH$_2$ (I4/mmm); Th$_4$H$_{15}$ (I-43d).

The experimental powder patterns along with the results of the refinement fit are shown in Fig. 2(a) and (b) for $(UTh_4Zr_{10})H_{1.9}$ and $(U_4Th_2Zr_9)H_{1.5}$ fuels, respectively. Structure factor calculations (SFC) were performed to match the experimental XRD intensities from different phases to the calculated volume fractions presented in Table 1. SFC was done specifically comparing the 0 2 2 type reflection from the ThZr$_2$H$_{7-x}$ phase and the 0 2 1 and 1 1 0 reflections from the α-U phase in the $(U_4Th_2Zr_9)H_{1.5}$ fuel. Scattering from hydrogen atoms was neglected in this calculation since the atomic scattering factor from this element is negligible compared to that of the other species. The resulting normalized intensities agree well with the experimental values (Table 3).

3.2. Scanning electron microscopy (SEM)

Scanning electron microscopy was performed on a JEOL instrument model JSM-5610 equipped with secondary and backscatter electron detectors and an Oxford ISIS EDS (energy dispersive X-ray spectroscopy) system. The accelerating potential during operation was 15 kV. Fig. 3 shows the backscattered electron image of the two fuels. The morphology of both fuels showed three distinct phases present. Each region corresponds to the one of the structures identified in the previous section, where the phases from brightest to darkest are α-U, ThZr$_2$H$_{7-x}$, and δ-ZrH$_{1.6+x}$, respectively. This is the case since the intensity of the backscattered image is proportional to the average atomic number in each phase. This is also in agreement with the corresponding EDS spectra.

Severe microcracking is observed in the microstructure of the $(UTh_4Zr_{10})H_{1.9}$ fuel, a result of volume expansion during processing. The cracks are both transgranular and intergranular, forming a network that expands across the microstructure. However, no sign of cracking is observed in the microstructure of $(U_4Th_2Zr_9)H_{1.5}$. This is in agreement with the calculated percent volume expansions of 22.4% and 17.7% upon hydriding for $(UTh_4Zr_{10})H_{1.9}$ and $(U_4Th_2Zr_9)H_{1.5}$ fuels, respectively. Solubility of thorium in the γ(U + Zr) phase and zirconium and uranium in the α-Th phase are assumed to be zero in this analysis. The volume expansion is then calculated based on the change in the molar volume of the phase prior to and after hydriding. The extent of cracking for $(UTh_4Zr_{10})H_{1.9}$ fuel significantly worsened over time after hydriding when the material was stored at room temperature. This is

Table 2
Lattice parameter of phases present in the $(UTh_4Zr_{10})H_{1.9}$ and $(U_4Th_2Zr_9)H_{1.5}$ fuels determined through Rietveld refinement.

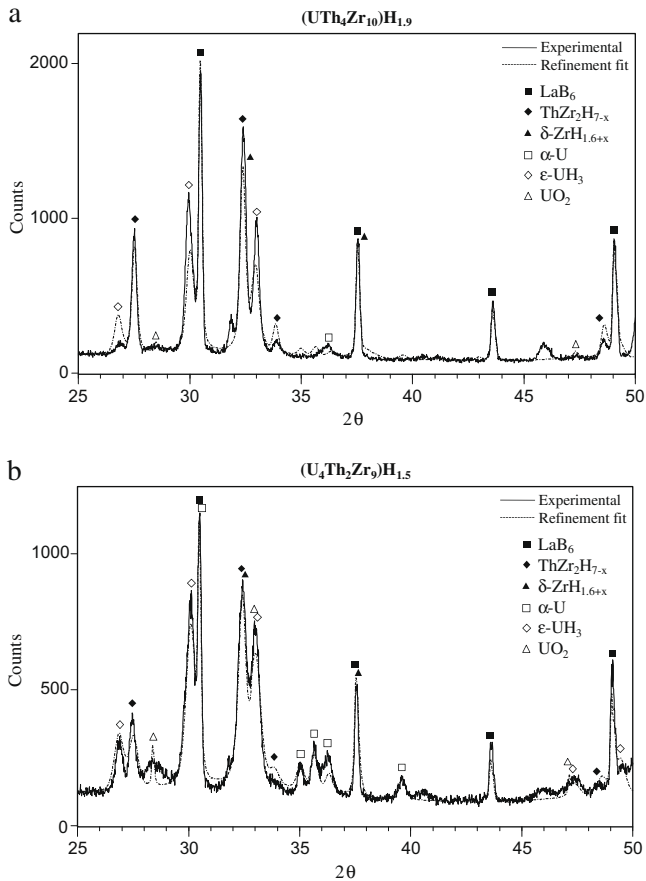| Phase	Space group	$(UTh_4Zr_{10})H_{1.9}$	$(U_4Th_2Zr_9)H_{1.5}$	Reference
ThZr$_2$H$_{7-x}$	Fd-3m	a = 0.9186 nm	a = 0.9184 nm	a = 0.9154 nm [10]
δ-ZrH$_{1.6}$	Fm-3m	a = 0.4783 nm	a = 0.4762 nm	a = 0.4777 nm [11]
α-U	Cmcm	N/A	a = 0.2855 nm	a = 0.2854 nm [12]
		N/A	b = 0.5862 nm	b = 0.5869 nm
		N/A	c = 0.4956 nm	c = 0.4955 nm
ε-UH$_3$	Pm-3n	N/A	a = 0.6655 nm	a = 0.6627 nm [13]

Fig. 2. Powder X-ray diffraction patterns for (a) $(UTh_4Zr_{10})H_{1.9}$ and (b) $(U_4Th_2Zr_9)H_{1.5}$ fuels along with Rietveld refinement fit.

Fig. 3. Backscattered electron image of (a) $(UTh_4Zr_{10})H_{1.9}$ and (b) $(U_4Th_2Zr_9)H_{1.5}$ fuels.

Table 3
Comparison of peak intensities between experimental results and structure factor calculations.

Phase	Reflection	Experimental	SFC
$ThZr_2H_{7-x}$	0 2 2	1	1
α-U	0 2 1	0.75	0.79
	1 1 0	0.32	0.27

due to residual stresses in the material. However no such behavior was observed in case of the $(U_4Th_2Zr_9)H_{1.5}$ fuel.

The morphology of both fuels shows elongated grains, but this feature is much more noticeable in the $(U_4Th_2Zr_9)H_{1.5}$ fuel. This morphology is due to the formation of dendrites during the solidification of metal alloys. Uranium particles are evenly dispersed in small scale in $(UTh_4Zr_{10})H_{1.9}$ fuel ($\leqslant 1$ μm in diameter) while in $(U_4Th_2Zr_9)H_{1.5}$ fuel the uranium particle distribution is random with large particle size. Similar characteristics can be seen for δ-$ZrH_{1.6+x}$ grains of different sizes with an average diameter in the range of a few micrometers. These micrographs further show that the ternary $ThZr_2H_{7-x}$ is the dominant phase in both fuels. This major chemical phase represents ~85 vol.% of the (UTh_4Zr_{10}) $H_{1.9}$ sample where it is continuous. On the other hand only ~46 vol.% of the $(U_4Th_2Zr_9)H_{1.5}$ sample constitutes this phase.

3.3. Transmission electron microscopy (TEM)

Transmission electron microscopy was performed using a TEC-NAI-G2-F30 microscope with a 300 keV field emission gun. TEM
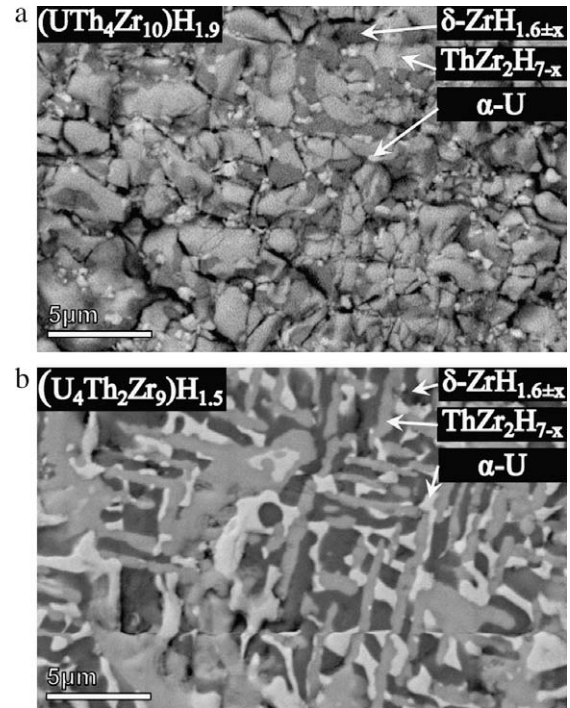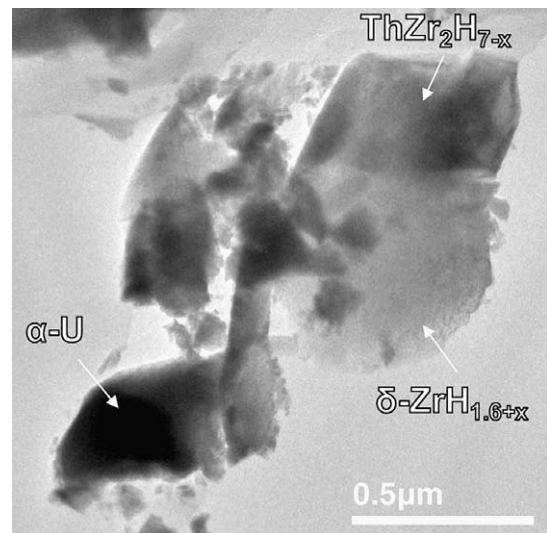

Fig. 4. Bright field image of $(U_4Th_2Zr_9)H_{1.5}$ fuel.

images were recorded using a low scan CCD camera attached to a Gatan GIF 2000 image filter. Four TEM specimens were prepared through microtome cutting at thicknesses of 25 and 50 nm for each fuel. Thin samples are essential because of the significant electron beam attenuation by samples consisting of high atomic number elements. Powdered fuel was initially embedded in spur-resin in a microvial, which was then solidified at 60 °C overnight. The microtome specimens were cut using the diamond blade of a Leica EM UC6rt instrument and were then placed on a 3 mm copper grid supported by a thin carbon film.

A bright field image of $(U_4Th_2Zr_9)H_{1.5}$ is presented in Fig. 4. This image lacks any morphological information since the specimens were prepared starting from fine powder, and during microtomy further cracking occurred. Dislocation-free grains of $ThZr_2H_{7-x}$
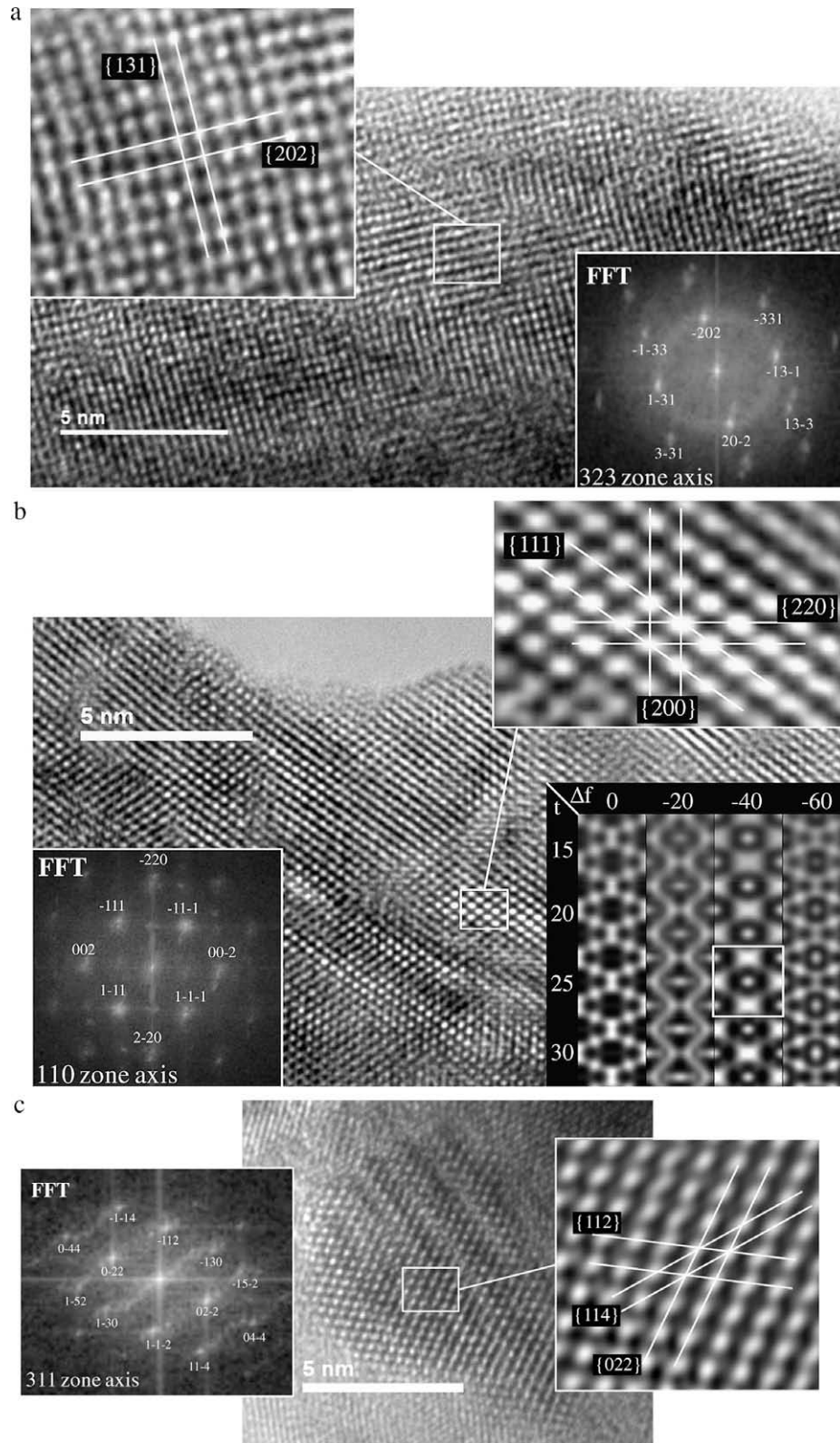
Fig. 5. Phase contrast imaging on $(U_4Th_2Zr_9)H_{1.5}$ fuel. (a) 323 zone axis of $ThZr_2H_{7-x}$ phase ($\Delta f = -100$ nm). (b) 110 zone axis of δ-$ZrH_{1.6+x}$ along with Bloch wave computer simulation ($\Delta f = -40$ nm). (c) 311 zone axis of α-U ($\Delta f = -60$ nm).

and δ-$ZrH_{1.6+x}$ phase are shown with good coherence at the grain boundary. EDS was performed by the TEM in scanning mode, confirming the composition of the grains shown in the image.

High-resolution (HRTEM) images of $ThZr_2H_{7-x}$, δ-$ZrH_{1.6+x}$, and α-U phases were generated through phase contrast imaging. The

microscope's spherical and chromatic aberration coefficients were reported as 1.2 mm and 1.4 mm by the manufacturer. Fig. 5 shows the phase contrast image of the three phases forming the fuels along with the fast Fourier transformation of each image into reciprocal space. The extent of defocus for the $ThZr_2H_{7-x}$ phase
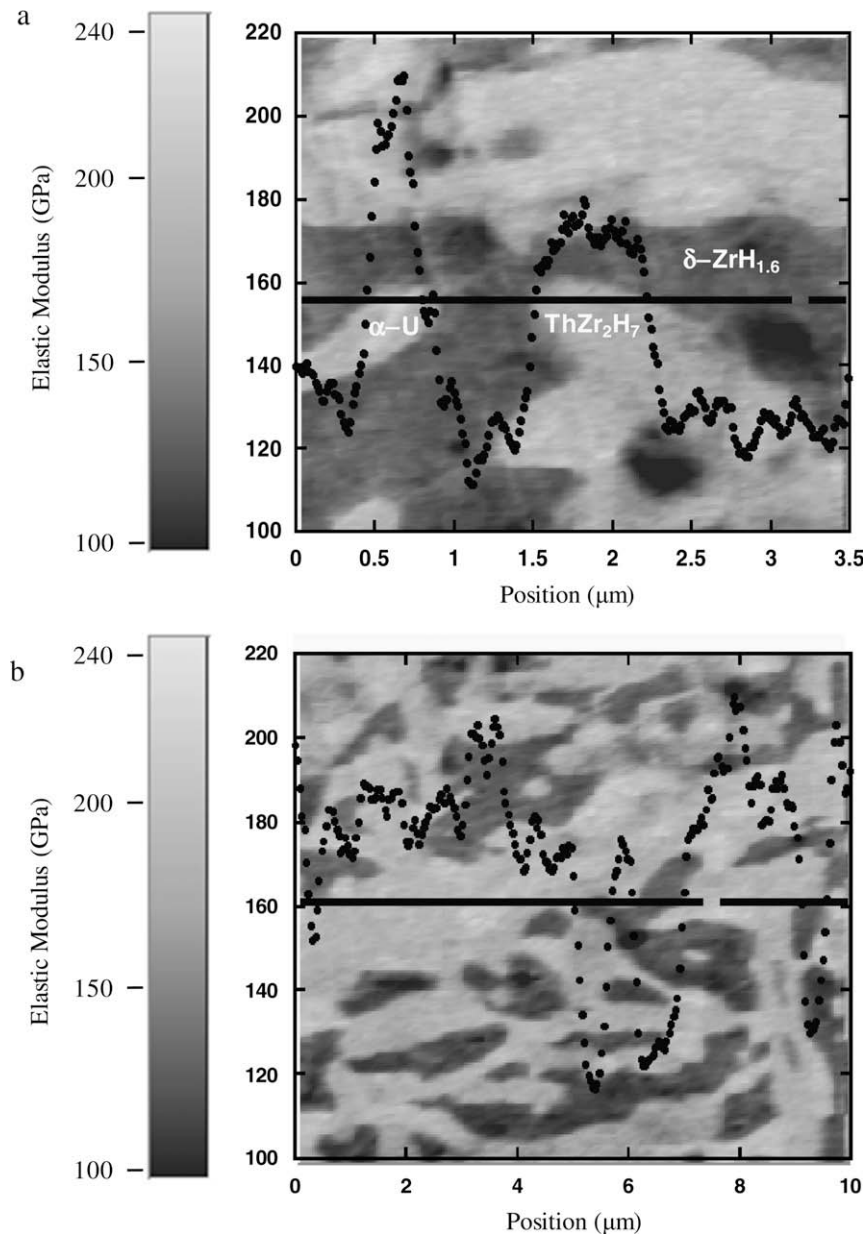
Fig. 6. Elastic modulus mapping across the microstructure of $(U_4Th_2Zr_9)H_{1.5}$ fuel (a) $3.5 \times 3.5\ \mu m^2$ area (b) $10 \times 10\ \mu m^2$ area.

contrast image is determined through analysis of contrast transfer function contours based on scattering from an amorphous region of the sample. No amorphous region was present during imaging of the δ-$ZrH_{1.6+x}$ or α-U phase, and Bloch wave computer simulation [14] was used instead to estimate the defocus value. This approach is shown in Fig. 5(b) where the phase contrast image of δ-$ZrH_{1.6+x}$ is matched by computer simulation at 25 nm sample thickness and −40 nm defocus.

The observations from HRTEM are in agreement with the XRD results, confirming the formation of $ThZr_2H_{7-x}$ and δ-$ZrH_{1.6+x}$. No sign of formation of tetragonal ϵ-$ZrH_{1.8}$ phase is observed. The FFT (fast Fourier transform) of the image corresponding to the uranium phase is representative of diffraction from an orthorhombic phase. This result rules out formation of significant amounts of cubic ϵ-UH_3.

3.4. Nanoscale dynamic stiffness mapping (DSM)

DSM (TriboScope nanoindenter, Hysitron, Minneapolis, MN) coupled with an atomic force microscope controller (NanoScope IIIa, Veeco, Santa Barbara, CA) was used to determine the elastic modulus of the phases forming the uranium–thorium–zirconium hydride fuels. The technique provides topography as well as viscoelastic properties through storage and loss moduli mapping across the fuel microstructure at nanometer length scales. This was done by applying a sinusoidal electrostatic force acting on the spring-suspended center of the force-displacement transducer of the nanoindenter while contact mode imaging was conducted. A cube-corner diamond tip was attached to this transducer. The amplitude and the phase of the resulting transducer displacement signal were measured with a dual-channel lock-in amplifier, and this information was used to determine the local indentation moduli of the sample at each pixel of the imaging process. In the present case only the storage modulus (designated as elastic modulus) is reported due to negligible magnitudes of loss modulus found for the samples studied. The diamond tip radius used for imaging was calibrated by a standard quartz sample with an elastic modulus of 69.7 GPa. Balooch et al [15] provide detailed description of the instrument and the technique.
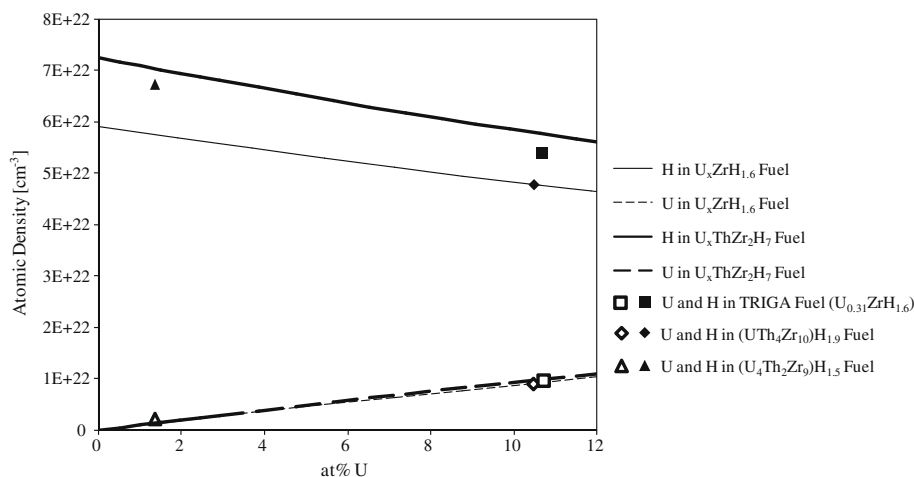
Fig. 7. Hydrogen and uranium atomic density as a function of at.% uranium metal in different hydride matrices.

Two regions of $3.5 \times 3.5 \ \mu m^2$ and $10 \times 10 \ \mu m^2$ area were investigated in the $(U_4Th_2Zr_9)H_{1.5}$ fuel, and the results are presented in Fig. 6(a) and (b), respectively. The elastic modulus values are represented by the shades of gray in the images. The variation of the elastic modulus (black spots) along the black horizontal lines superimposed on the images is also shown for further clarification. Three distinct regions, corresponding to α-U, $ThZr_2H_{7-x}$, and δ-$ZrH_{1.6+x}$, are apparent from brightest to darkest, respectively. The microstructure in this set of images is directly comparable to what was previously characterized during backscattered scanning electron microscopy.

The elastic moduli of α-U and δ-$ZrH_{1.6+x}$ are reported as 202 GPa [16] and 130 GPa [17], respectively. The results of this study are in good agreement with the values reported previously for these two phases. The elastic modulus of the ternary $ThZr_2H_{7-x}$ phase has not been reported previously and the mean value is determined here as 172 ± 5 GPa.

4. Discussion

Fuel fabrication could be improved by homogenization of the arc-melted metal alloys prior to hydriding in order to remove the dendritic structure. The hydriding process could also be greatly improved if the desired H/M ratio is initially established at high temperature and then maintained during the cool-down. The diffusion-limited process takes place relatively quickly at high temperature under high pressure of hydrogen gas while the material is ductile enough to accommodate the large volume expansion. During the cool-down step, the hydrogen partial pressure should be continuously reduced to correspond to the desired H/M ratio. This inhibits formation of hydrogen concentration gradients that would in turn induce stress across the material. The equilibrium partial pressure of hydrogen with zirconium hydride and thorium–zirconium hydride is known [18,19] as a function of temperature. At equilibrium, the activity of hydrogen in the gas and the two hydride phases is identical; therefore the exact H/M ratio in each phase could be determined. However, the equilibrium partial pressure of hydrogen changes by four orders of magnitude over the processing temperatures of these hydrides. Therefore, sophisticated instrumentation and control systems are necessary to execute this procedure.

The thermodynamic stability of the possible metal hydrides in this system increases as follows: UH_3, ThH_2, δ-$ZrH_{1.6+x}$, $ThZr_2H_{7-x}$ [20–24]. However, the thermodynamic stability changes as a function of H/M ratio. This result is in agreement with the characterization observations, where only the latter two hydrides were observed. Uranium hydride is unstable above 420 °C (under

1 atm of H_2 gas). The residual uranium hydride formation, as detected by XRD analysis, is due to the presence of hydrogen in the furnace during the cool-down.

The actual H/M ratio in the $ThZr_2H_{7-x}$ phase is unknown. Bartscher et al. [10] have studied the $ThZr_2D_x$ system using neutron scattering and report the lattice parameter for the cubic unit cell as a function of different deuterium to metal ratios up to 6.3. Linear extrapolation of these results matches the determined lattice parameter of this phase to hydrogen stoichiometry of 7 (as in $ThZr_2H_7$) in both fuels.

The density of hydrogen in hydride nuclear fuels is of great importance since it replaces a part of the moderator and thus significantly affects the neutronic properties. Fig. 7 shows the hydrogen and uranium atomic densities in different hydride fuels as a function of atomic percent uranium dispersed in the hydride matrix. Uranium–thorium–zirconium hydride fuels are superior to uranium–zirconium hydride fuels since similar uranium atomic densities could be achieved with higher hydrogen atomic densities.

5. Conclusions

Two uranium–thorium–zirconium alloys were arc-melted and then hydrided to form fuels with the nominal compositions of $(UTh_4Zr_{10})H_{1.9}$ and $(U_4Th_2Zr_9)H_{1.5}$. Powder XRD analysis showed both these fuels consisted of the α-U, δ-$ZrH_{1.6+x}$, and $ThZr_2H_{7-x}$ phases with the latter being dominant in both. SEM and TEM (in bright field and high-resolution mode) imaging confirmed the presence of these three phases. Atomic force microscopy along with nanoscale dynamic stiffness analysis performed on fuel specimens to map the Young's modulus across the microstructure revealed the elastic modulus of $ThZr_2H_{7-x}$ to be 172 ± 5 GPa.

Uranium–thorium–zirconium hydride fuels appear to be superior to TRIGA fuel for power reactor use since the hydride matrix is more stable with respect to dehydriding. Also, high uranium and hydrogen atomic densities are achieved in fuels containing thorium. Extensive study of the effects of irradiation on these fuels under typical light water reactor conditions is necessary in order to adequately understand their performance compared to TRIGA and oxide fuels.

References

[1] F. Ganda, E. Greenspan, Nucl. Sci. Eng. (2009).
[2] F. Ganda, E. Greenspan, Plutonium incineration capability of hydride versus MOX fuel in PWR, in: Proceedings of the Global '05, Tsukuba, Japan, October 2005.
[3] F. Ganda, E. Greenspan, Incineration of plutonium in PWR using hydride fuel, in: Proceedings of the 2005 International Conference on Advances in Nuclear Power Plants ICAPP-2005, Seoul, Korea, May 2005.
[4] F. Ganda, E. Greenspan, Nucl. Eng. Des. (2009).
[5] F. Ganda, E. Greenspan, Nucl. Eng. Des. (2009).
[6] F. Ganda, E. Greenspan, Plutonium and Minor Actinides Multi-recycling in PWR Using Hydride Fuels, Physor 2008, Interlachen, CH, 2008.
[7] T. Yamamoto, H. Suwarno, H. Kayano, M. Yamawaki, J. Nucl. Mater. 247 (1997) 339.
[8] T.A. Badaeva, G.K. Alekseenko, Struct. Alloys Certain Syst. Cont. Uranium Thorium (1963) 376.
[9] B. Tsuchiya, J. Huang, K. Konashi, W. Saiki, T. Onoue, M. Yamawaki, J. Alloys Compd. 312 (2000) 104.
[10] W. Bartscher, J. Rebizant, A. Boeuf, R. Caciuffo, F. Rustichelli, J. Fournier, W. Kuhs, J. Less Common Met. 121 (1986) 455.
[11] R. Beck, Trans. Am. Soc. Met. 55 (1962) 542.
[12] E.F. Sturken, Acta Crystallogr. 13 (1960) 852.
[13] W. Bartscher, A. Boeuf, R. Caciuffo, J. Fournier, W. Kuhs, J. Rebizant, F. Rustichelli, Solid State Commun. 53 (1985) 423.
[14] J.M. Zuo, J.C. Mabon, Microsc. Microanal. 10 (Suppl. 2) 2004; URL: <http://emaps.mrl.uiuc.edu/>.
[15] G. Balooch, G. Marshall, S. Marshall, O. Warren, S. Asif, M. Balooch, J. Biomech. 37 (2004) 1223.
[16] ASM Handbooks, vol. 2, Properties and Selection: Nonferrous Alloys and Special-Purpose Materials.
[17] S. Yamanaka, K. Yoshioka, M. Uno, M. Katsura, H. Anada, T. Matsuda, S. Kobayashi, J. Alloys Compd. 293–295 (1999) 23.
[18] M. Simnad, Nucl. Eng. Des. 64 (1981) 403.
[19] K. Konashi, B. Pudjanto, T. Terai, M. Yamawaki, J. Phys. Chem. Solids 66 (2005) 625.
[20] C.J.M. Northrup Jr., J. Phys. Chem. 79 (1975) 726.
[21] E. Wicke, K. Otto, Z. Phys. Chem., Neue Folge 31 (1962) 222.
[22] M.W. Mallett, I.E. Campbell, J. Am. Chem. Soc. 73 (1951) 4850.
[23] W. Wang, D.R. Olander, J. Am. Ceram. Soc. 78 (1995) 3323.
[24] W. Bartscher, J. Rebizant, J. Less Common Met. 136 (1988) 385.